Patient-level Prediction of Multi-classification Task at Prostate MRI based on End-to-End Framework learning from Diagnostic Logic of Radiologists

Lizhi Shao, Zhenyu Liu, *Member, IEEE*, Ye Yan, Jiangang Liu, Xiongjun Ye, Haizhui Xia, Xuehua Zhu, Yuting Zhang, Zhiying Zhang, Huiying Chen, Wei He, Cheng Liu, Min Lu, Yi Huang, Kai Sun, Xuezhi Zhou, Guanyu Yang, *Member, IEEE*, Jian Lu, Jie Tian, *Fellow, IEEE*

Abstract—The grade groups (GGs) of Gleason scores (Gs) is the most critical indicator in the clinical diagnosis and treatment system of prostate cancer. End-to-end method for stratifying the patient-level pathological appearance of prostate cancer (PCa) in magnetic resonance (MRI) are of high demand for clinical decision. Existing methods typically employ a statistical method for integrating slice-level results to a patient-level result, which ignores the asymmetric use of ground truth (GT) and overall optimization. Therefore, more domain knowledge (e.g. diagnostic logic of radiologists) needs to be incorporated into the design of the framework. The patient-level GT is necessary to be logically assigned to each slice of a MRI to achieve joint optimization between slice-level analysis and patient-level decision-making. In this paper, we propose a framework (PCa-GGNet-v2) that learns from radiologists to capture signs in a separate two-dimensional (2-D) space of MRI and further associate them for the overall decision, where all steps are optimized jointly in an end-to-end trainable way. In the training phase, patient-level prediction is transferred from weak supervision to supervision with GT. An association route records the attentional slice for reweighting loss of MRI slices and interpretability. We evaluate our method in an in-house multi-center dataset (*N*=570) and PROSTATEx (*N*=204), which yields five-classification accuracy over 80% and AUC of 0.804 at patient-level respectively. Our method reveals the state-of-the-art performance for patient-level multi-classification task to personalized medicine.

Index Terms—Gleason score, prostate cancer, patient-level prediction, joint optimization, MRI, reinforcement learning

I. Introduction

Prostate cancer (PCa) is the second most frequently diagnosed cancer for males worldwide, being one of the leading causes of cancer death among men [1]. The grade group (GG) of Gleason score (Gs) [2] reflects the biological behavior of tumors and remains the most powerful parameter to predict cancer survival [3] and guide treatment options [4], which are divided into five groups from 1 (best) to 5 (worst) by the latest criteria of the International Society of Urological Pathology [5]. GG of a patient helps clinicians choose appropriate decisions throughout the primary diagnosis, preoperative plan and postoperative treatment of prostate cancer treatment for personalized medicine. Clinically, current treatment options mainly depend on a patient-level GG from needle biopsies (NB) (GG-NB) [3]. The GG of radical prostatectomy (RP) (GG-RP) evaluated from a set of whole-organ slices is the gold standard for pathological evaluation of PCa. However, discrepancies

between GG-NB and GG-RP are incredibly high, which remarkably reduces the reliability and credibility of clinical treatment decisions. The consistency rate between GG-RP and GG-NB is reported as low as 40%-57% [6, 7], which limited application of the model with GG-NB as the gold standard. Further opportunities to optimize treatment should be researched, such as multi-classification model with ground truth (GT) of GG-RP for predicting patient-level GG.

Magnetic resonance imaging (MRI) as a main diagnostic modality for PCa has shown the potential in clinical practice [8] for assessment of prostate lesions. T2 weighted imaging (T2WI) of MRI as the critical modality revealed the main potential for detecting tumors and differentiating characteristics of tumors. However, we still cannot obtain enough accurate evaluation from images relying on qualitative or semi-quantitative MRI-based evaluation methods of the clinic. Deep convolutional neural network (DCNN)-based methods reveal exciting performance in slice-level prediction by pixel-wise analysis [9, 10]. Furtherly, due to the limited inter-slice resolution of prostate MRI and the particularity of multiple foci in PCa, patient-level multi-classification tasks of MRI refer to combine slice-level results to obtain an overall conclusion, which poses new challenges to previous methods that only focused on slice-level analysis.

Hierarchical predicting GG-RP of a patient has always been a significant challenge for precision treatment [11] in PCa. Clinically, radiologists firstly explore signs from two-dimensional (2D) images as slice-level analysis and then associate slice-level diagnosis for a patient-level conclusion. The most challenging problems of DCNN-based method of slice-level are as follows: (1) how to perform quantitative image analysis for each slice in the MRI of prostate, (2) how to eliminate the interference of redundant information on weak supervision, (3) how to transfer slice-level results to a patient-level conclusion, and (4) how to make the decision-making process fit the logic of clinical workers for interpretability.

Our contributions are summarized as follows:

1. We design an end-to-end framework for patient-level multi-classification tasks, which diagnostic logic of radiologists was fully learned and applied in modeling for better performance and interpretability.

2. GG-RP is used as the GT for the first time to pointedly predict the pathological grade of PCa patients.

3. A dual attention network is designed for PCa to better pixel-wise analysis in the slice-level, and A DRL-based network is designed for joint optimization.

4. A strategy to re-weight the importance of slices (RWIS) in training is devised.

5. We evaluate our framework in both an in-house multi-center dataset (PCa-GGDATA) and an open dataset (PROSTATEx).

II. RELATED WORK

DCNNs are popular for pixel-wise analysis and have shown the potential for application to PCa problems, including classification [9, 10, 12, 13], organ or lesion segmentation [13-16], and registration [17]. These studies were mainly based on weakly supervised learning [9, 12, 18], which refers to the establishment of relations between GTs of patients and each slice of MRI as a supervised label. The GTs are from different sources for specific clinical applications: PI-RADS scores, GG-NB, and GG-RP. Yang et al. and Wang et al. [9, 18] proposed a CNN-based framework to detect clinically significant prostate cancer (sPCa) in mp-MRI. The method identifies sPCa and lesions simultaneously using the consistency loss of different modal feature maps under only category supervision information (biopsy-proven Gs). Schelb et al. [12] combined T2WI and diffusion-weighted imaging (DWI) to detect and segment suspicious lesions that could indicate significant PCa. Due to the requirements of clinical applications, models with neither PIRADS-proven nor NB-proven GT are not suitable for directly predicting RP pathology. Therefore, Cao et al. [15] used an improved multi-class DCNN to jointly detect RP-proven PCa lesions and predict the GGs from mp-MRI. This is the first study conducted to train or validate a DCNN for PCa detection at a slice-level from RP pathology.

However, in these studies, it is difficult to integrate slice-level predictions into a patient-level result through a vote-based strategy (e.g., majority-vote, mean, or maximum), by using DCNN alone. Additionally, three-dimensional (3D) DCNN-based models with massive parameters and a high computational cost are also inappropriate for abdominal MRI of low inter-slice resolution. For accuracy, decision logic, and clinical applications, we need a more elegant way to take advantage of pixel-wise analysis for patient-level tasks.

Recent studies have shown that deep reinforcement learning (DRL) can potentially achieve final goals through actions of frames and be a bridge of joint optimization [19]. Mnih et al. [20] first proposed a deep Q-learning network (DQN) to simulate human behavior to compete in e-sport games. Actions are generated from encoding features of DCNNs with a higher reward. This work was then extended into the medical field for automated anatomical landmark searching [21] and lesion detection [22, 23] on DCE-MRI. The DRL was used to determining coordinates of locations within image blocks. However, to our knowledge, no model is applying DRL to learn from diagnostic logic of radiologists for modeling, especially for multi-classification tasks at the patient-level.

Some studies also tried radiomics methods [24] to perform patient-level analysis for predicting pathological behavior by extracting quantitative hand-crafted image features in MRI of PCa [25] directly. However, the PCa with limited radiological detection for low-volume foci brings a huge challenge to lesion segmentation, which reduces the repeatability of features extracted from MRI and restricts reliability of the models. Additionally, heavy labeling works also limits the scale of data involved in modeling.

Clinically, the patient-level diagnosis of PCa in MRI-based examinations is constructed with slice-level evaluations. However, a single sequence of MRI examinations of a patient usually contains almost twenty or more slices with low inter-slice resolution, which complicates decision-making. Radiologists use their experience to find the diagnosis-related slices and deduce a series of inferences to draw a patient-level decision [26]. Our previous study tried to combine DCNN with
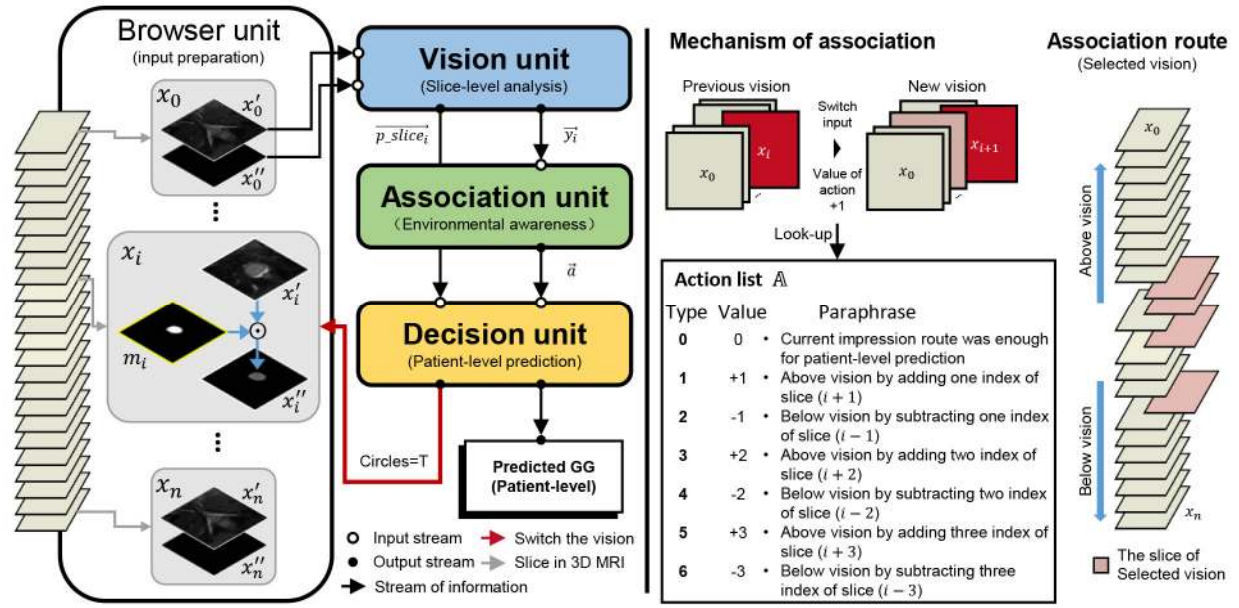
Fig. 1. Workflow of PCa-GGNet-v2. PCa-GGNet-v2 for predicting GG-RP of patient-level (right). Mechanism of association for visions and association route for re-weighting slices during weak supervision of vision unit (left).

DRL to build a model (PCa-GGNet) for predicting GG-RP [27], which effectively reduces the risk of up- and down-regulation in the pathological assessment of biopsy. However, the framework lacks sufficient attention to the tumor area in slice-level and joint optimization. From previous research experience, image features will directly affect the decision path selection of the model, and then affect the final model performance. At the same time, there is a lack of methodological evaluation and comparison of international public data.

III. FRAMEWORK METHODOLOGY

The proposed framework consists of concatenated subunits: 1) a browser unit for input preparation; 2) a vision unit (VU) for slice-level predictions and visual features extraction; 3) an association unit (AU) for reasoning and analysis area switching between slice-level results; 4) a decision unit (DU) for determining a patient-level prediction from series of slice-level predictions. As shown in **Fig. 1**, our proposed framework (PCa-GGNet-v2) $P(X)$ aims to construct a patient-level prediction for five-tier GG-RP in an end-to-end approach. The inputs are image areas of both prostate and tumor in T2WI $X = \{x_1, x_2, \ldots, x_n\}$. Three arithmetic units were defined by $V(x; \theta_{P1}, \theta_{P2}, w_O, w_T, w_F)$, $A(\vec{y}; w_A)$, $D(\vec{a})$, respectively. The VU analyzes slices x by DCNN-based model, focuses on the character of the lesion in planar spatial information and environment of the prostate, and provides materials $\{Y, P_{slice}\}$ (feature vectors of slices $Y = \{\vec{y_1}, \vec{y_2}, \ldots, \vec{y_n}\}$; slice-level prediction vectors of slices $P\_slice = \{\overrightarrow{p\_slice_1}, \overrightarrow{p\_slice_2}, \ldots, \overrightarrow{p\_slice_n}\}$) as inputs to the DU. The AU is developed by DQN. Using feature $\vec{y}$, it moves by an action probability vectors $\vec{a}$ to switch the vision. The action is defined by $\mathbb{A}(\text{argmax}(\vec{a}))$, where $\mathbb{A}$ is the action list. The selected slices from actions are defined as an association route R. The last unit is DU, which takes responsibility for the prediction of patient-level GG-RP $\mathbb{P} = \text{argmax}(\overrightarrow{p\_case})$. Here, $\overrightarrow{p\_case}$ is a probability vector of GG-RP, which is the same as the prediction of the current vision. The DU decides when to shut down the framework. Our PCa-GGNet-v2 is a recurrent architecture and continues until the status of the prediction satisfies the termination condition. For cycles $t \in [1, \text{T}]$, we update the input image $x_{i+\mathbb{a}_t}$ of the VU according to the action to realize the next cycle $t + 1$. The patient-level prediction of GG-RP $\mathbb{P}$ is captured from the terminal point of the framework. The patient-level prediction of GG-RP by PCa-GGNet-v2 is defined as

$$P(X) = D\big(A(V(X; \theta_{P1}, \theta_{P2}, w_O, w_T, w_F); w_A)\big) \quad (1).$$

A. VU with dual attention for multi-classification of slice-level

We firstly build the VU for pixel-wise analysis of 2D images as slice-level analysis. **Fig. 3** shows a schematic illustration of the VU. The backbone of the VU is PNASNet [35]. The PNASNet is created by a progressive search strategy, which is sequential model-based optimization. Cell blocks (Cells) of the PNASNet help avoid the vanishing gradient problem within lower layers of DCNN during the training phase. It also enables the model to associate different low-level features with deeper convolutional (high-level) features.

The input layer of VU requests a set of images x, including prostate image x' and tumor image x''. The tumor image is obtained by convolution of the prostate x' and the tumor mask m.

$$x'' = x' \odot m \quad (2)$$

Two PNASNet-based models without the last connection layer were parallel, which PNASNet-1 $F_{P1}(x', \theta_{p1})$ and PNASNet-2 $F_{P2}(x'', \theta_{p2})$ analyzes image information from the prostate area and tumor area respectively.

The PNASNet-based models serve as a non-linear function to encode the image into a sparse matrix named deep maps m_O and m_T, representing feature maps of prostate (organ-level) and lesion (tumor-level), which are defined as

$$m_O = F_{P1}(x', \theta_{p1}) \quad (3),$$

$$m_T = F_{P2}(x'', \theta_{p2}) \qquad (4).$$

The last feature maps of two branches are transformed into focal features m_F for focal attention (Focal-level), which is defined as

$$m_F = m_O \odot m_T \qquad (5).$$

Then, the average pooling with filter size of 11×11 serves as a dimensionality reduction function to encode the features into fixed-length vector representations $\overrightarrow{y_O}$ (organ-level), $\overrightarrow{y_T}$ (tumor-level), and $\overrightarrow{y_F}$ (Focal-level), respectively. The vector with probabilities of slice-level prediction $\overrightarrow{p\_slice}$ is integrated by three levels of predictions, which is defined as

$$\overrightarrow{p\_slice} = \overrightarrow{p\_slice_O} + \alpha * \overrightarrow{p\_slice_T} + \beta * \overrightarrow{p\_slice_F} \quad (6).$$

Weights of predictions from tumor-level and focal-level are defined by $\alpha \in [0,1]$ and $\beta \in [0,1]$. If the input x is missing the tumor mask m, α and β are both set 0.

Outputs of three-level predictions by a fully connected layer $F_{last}(\cdot)$ with parameters w, and is activated by a sigmoid function $\sigma_{Sigmoid}(\cdot)$. The outputs functions are defined as

$$\overrightarrow{p\_slice_O} = \sigma_{Sigmoid}\big(F_{last}(\overrightarrow{y_O}; w_O)\big) \qquad (7),$$

$$\overrightarrow{p\_slice_T} = \sigma_{Sigmoid}\big(F_{last}(\overrightarrow{y_T}; w_T)\big) \qquad (8),$$

$$\overrightarrow{p\_slice_F} = \sigma_{Sigmoid}\big(F_{last}(\overrightarrow{y_F}; w_F)\big) \qquad (9).$$

We used the VU to generate deep features $\vec{y}$ of each slice for slice-level prediction $\overrightarrow{p\_slice}$, tumor slice searching, and patient-level results construction.
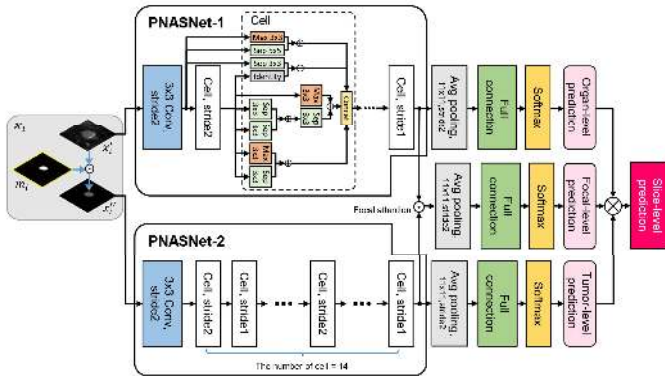

Fig. 2. Architecture of the VU.

B. AU for environmental awareness and tumor slice searching

We build the AU to perceive the complete image environment of T2WI, and find a decision path for patient-level decision, which is composed of tumor slices. Inspired by behavioral psychology, RL can be learned by interaction with environments to maximize cumulative reward signals [28]. When a radiologist examines the MRI of the prostate, switching between slices of observations is a necessary process [26]. The result of a patient is obtained by combining the browsing path and association, which is the decision path named as an association route in our study. If a single sequence is not sufficiently reliable for diagnosis, additional sequences will be included. In our study, we mimic the process and create a learning agent (the AV) A. The agent works in environment E

and makes an action $\mathbb{a}$ based on variable status s (encoding features of each slice) to build a slice list named association route R. The destination of the association route points a patient-level probability vector $\overrightarrow{p\_case}$. The final patient-level predicted signature $\mathbb{P}$ is defined as $\mathbb{P} = argmax(\overrightarrow{p\_case})$.

The DQN [20] is employed as the backbone for the AU, including a CurrentNet $A_{current}(s, a; w_c)$ and a TargetNet $A_{target}(s, a; w_t)$. The CurrentNet only learns and updates during the training phase. In testing, there is only the TargetNet for action making. The agent will not receive any rewards nor update the model; it only follows the learned policy. The workflow and definition of architecture for the AU is illustrated in **Fig. 3**. The details of action $\mathbb{a}$ and states s for the agent are introduced as follows.

1) Navigation Actions

The agent takes the action steps $\mathbb{a}$ to interact with E, which implies a change of input for the framework. Slice with tumor is defined as an attentional slice $x_{attention}$. The action list $\mathbb{A}$ is composed of seven actions $\{0, +1, +2, +3, -1, -2, -3\}$, which indicates the direction of movements and the step length. The positive numbers indicate the direction of the seminal vesicle gland and negative numbers toward the perineum. Action type of zero is represented as "Stay at the place," which is a stop order, and the attentional slice $x_{attention}$ is not updated during the testing.

2) Environments and States

Environment E represents the feature group of all slices of a T2WI, where each state s is an encoded feature $\vec{y}$ from the VU. During the training phase, the environment also contains the probability of slice-level prediction $\overrightarrow{p\_slice}$ to evaluate reward r for each status-based action.
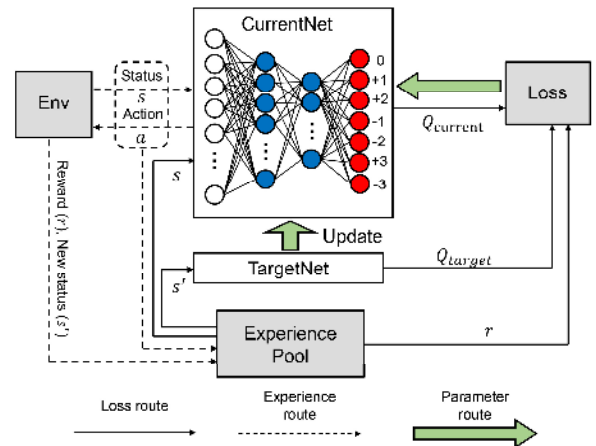
Fig. 3. Workflow of the AU.

C. DU for patient-level decision

DU $D(\overrightarrow{p\_slice}, \mathbb{a})$ is followed by the AU and is responsible for the prediction of patient-level $\mathbb{P}$. It is established for the framework to stabilize the search routes and prevent getting stuck in repeated cycles. When $\mathbb{a} = 0$, the association route satisfies patient-level prediction, and the patient-level prediction is inherited from the slice-level prediction of this slice. $\overrightarrow{p\_slice_{\mathbb{a}}}$ denotes slice-level prediction corresponding to the action $\mathbb{a}$. An experienced timepoint (T_{et}) is used to capture
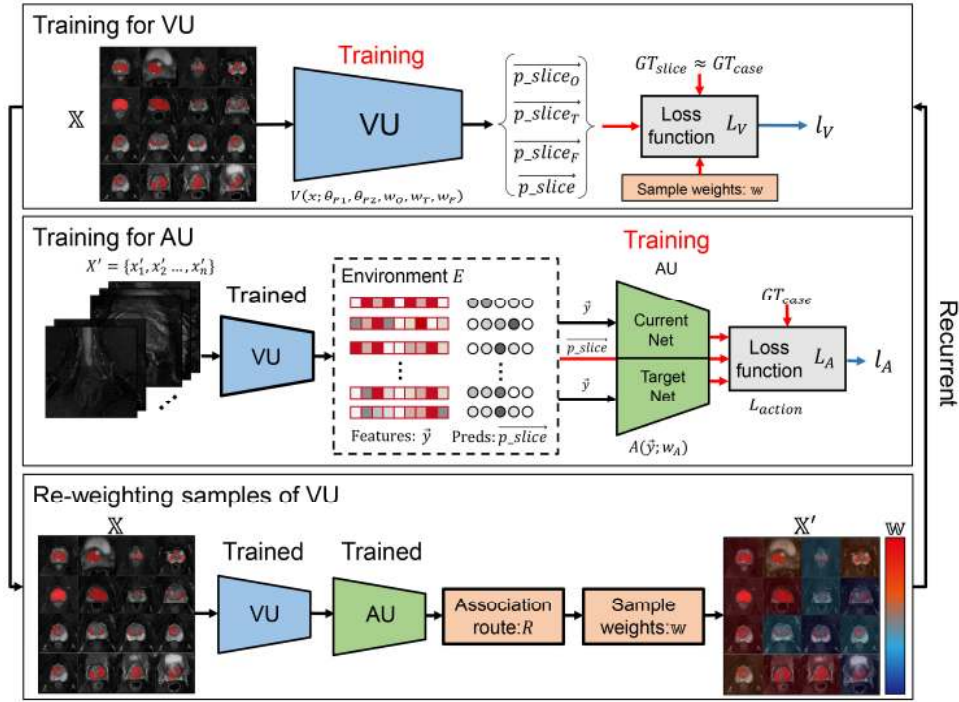
Fig. 4. Training for Pca-GGNet-v2.

the T_{et} action steps by the framework in searching for the prediction of patient-level GG-RP. The $\mathbb{P}$ is defined as follows.

$$\mathbb{P} = D\left(\overrightarrow{p\_slice_{\mathbb{a}}}, \mathbb{a}\right) =$$
$$\begin{cases} \text{argmax}\left(\overrightarrow{p\_slice_{\mathbb{a}}}\right), & \mathbb{a} = 0 \\ \text{argmax}\left(\overrightarrow{p\_slice_{\mathbb{a}_{T_{et}}}}\right), & \mathbb{a} \neq 0 \text{ and } t \geq T_{et} \end{cases} \quad (10)$$

The DU keeps the framework running until the given termination conditions.

IV. EXPERIMENTS

A. Training process

We reduce the coupling between the VU and the AU so that arithmetic units could be trained and evaluated independently. In the training process, the fitting of the two units influences each other actively. We alternately train the VU and the AU to improve the overall performance of the framework. The VU adopts weakly supervised learning strategy by minimizing the loss of the VU l_V to associate image representation with GG-RP. A trained VU then provides a training environment for the AU. AU packs each slice of 3D-T2WI as a training object with GT to realize supervised training by minimizing action loss l_A. The framework with the trained VU and AU generates an association route R by footprints of actions. It re-weighs the loss of inputs $\overrightarrow{w} = (w_1, w_2, . . , w_K)$ for training VU. The PCa-GGNet-v2 builds a bridge between an identified slice of image and patient-level GG-RP, which realizes end-to-end training based on the pixel-wise analysis and joint optimization. **Fig. 4** shows a schematic illustration of the framework training.

1) Training for the VU

First, we train the VU to classify GG-RP by pixel-wise analysis at the slice-level. Model parameters of the basic network, which is trained by ImageNet [29], are used as a pretrained network for transfer learning. During the training phase, the parameters of the PNASNet-1 and PNASNet-2 are frozen until the last Cells. Then, the VU is trained by weakly supervised learning, and labels of slices copy from the patient-level GG-RP. The loss of the VU l_V is defined as

$$l_V = l_{slice} + 0.1 * (l_O + \alpha * l_T + \beta * l_F) \quad (11).$$

The classification loss of prediction of organ-level, tumor-level, focal-level, and slice-level are l_O, l_T, l_F, and l_{slice}, which are cross-entropy.

To mitigate overfitting, data augmentation of random rotation, mirror transformation, and affine transformation are necessary to employ in the training. The masks of tumors for dual attention are randomly blinded. We select the organ region by a window size of 200×200 in the center area as the ROI to build the attention on the prostate, and the ROI is then scaled to 331×331 as the input.

2) Training for the AU

The second step of the PCa-GGNet-v2 is training for the TargetNet of the AU $A(\vec{y}, w_A) = A_{target}(\vec{y}, w_t)$, which $\vec{y}$ is set by features of the organ-level. The CurrentNet and TargetNet are spatially parallel with time delay. Parameters w_A of the TargetNet are updated by another model named CurrentNet $A_{current}(\vec{y}, w_c)$ with the same design as the TargetNet. The CurrentNet is used for experience $\mathcal{E} = \{s, \mathbb{a}_c, r, s'\} \in \mathbb{E}$, which is generated from the trained VU using a set of slices $X = \{x_1, x_2, . . . , , x_k\}$. Here, k denotes the number of slices per T2WI. The function of reward $\mathcal{R}(L, \overrightarrow{p\_slice}) = \mathcal{R}(\vec{g}, z, \overrightarrow{p\_slice})$ is defined as follows.

$$\mathcal{R}(\vec{g}, z, \overrightarrow{p\_slice}) =$$
$$\begin{cases} 1 + \sum_{k=0}^{K-1} g_k p\_slice_k & , \quad c(\vec{g}, \overrightarrow{p\_slice}) = 0 \text{ and } z = 1 \\ 1 & , \quad z = 1 \\ 0 & , \quad Other \end{cases} \quad (12)$$

Here, we define $c(\vec{g}, \overrightarrow{p\_slice})$ as $argmax(\vec{g}) - argmax(\overrightarrow{p\_slice})$. The GT encoded vector of GGs $\vec{g} = (g_1, g_2, g_3, g_4, g_5) \in \{0,1\}$ and GT of tumor existence for current slice $z \in \{0,1\}$ is in the goal list L for the reward. The limitation of greedy policy randomly chooses action $\mathbb{a}$, ignoring the real model output. The rate of random action was 0.9 during the training.

When the experience pool reaches overflow (N=2000), we randomly select a subset (N=256) of experiences for CurrentNet learning. The error is the difference between the current earnings $Q_{current}$ and future earnings Q_{traget}.

$$L_a(\mathcal{E}) = \left\| r + \gamma \max_{a'} A_{target}(s'; w_t) - A_{current}(s; w_c) \right\|^2 \quad (13)$$

where r is the reward corresponding to the current status; γ controls the influence of actions on the agent named learning rate, which was 0.9. The Adam optimizer with a basic learning rate of 0.01 was employed for the fitting.

In the process of experience collection, we take each experience pool overflow as a short period to conduct the CurrentNet training. A normal training cycle includes 100 short cycles, and the TargetNet updates by the CurrentNet. When the slice corresponding to the next action contains tumor presence markers and is consistent with the GT, a new environment E is selected for training. We also improve the richness of the environment to mitigate overfitting by the normal distribution mode centering on the middle layer to randomly select the initial state of the environment.

3) Re-weighting samples for training VU under Weak supervision

The strategy named re-weighting the importance of slices (RWIS) is generated by attentional slices of the AU, and the weights are named impression weights $\mathbb{w}$. We use $\mathbb{w}$ for VU training. The impression weights $\mathbb{w}$ are generated by attentional weights $\mathbb{w}'$ and results of slice-level prediction $\mathbb{w}''$.

$$\mathbb{w} = \mathbb{w}' + \mathbb{w}'' \quad (14)$$

Proportion of the times of the slice as an attentional slice $x_{attention}$ to the total slices of a T2WI is denoted as the attentional weight $\mathbb{w}'$. The $\mathbb{w}'$ was defined as follows.

$$\mathbb{w}' = \frac{Times\ of\ a\ slice\ as\ x_{attention}}{Total\ slices\ of\ a\ T2WI} \quad (15)$$

The impression weight of multi-rounds $\mathbb{w}_{d+1}$ for the circle $d \in [1, D]$ VU training is defined as

$$\mathbb{w}_{d+1} = \lambda \mathbb{w}_{d-1} + \mathbb{w}_d. \quad (16)$$

The weights of all training slices are initialized to 1 in the first training. λ controls the effect of impression weight. The influence of the early weight decreases with the increase in the number of training cycles of the framework. Next, in the VU training, we assign weights to the loss of the corresponding sample for loss construction $\mathbb{w} \odot l_V$, thereby purposefully emphasizing some training samples to enhance the VU. The AU then benefits from a better previous unit because of the higher quality of features expression and slice-level prediction.

B. Datasets

Pre-operative MRI data from 575 patients who later underwent both NB and RP were included in the study as in-house multi-center datasets (PCa-GGDATA). These patients are retrospectively enrolled in two Chinese hospitals, and includes three datasets of PUTH-p1, PUTH-p2, and PUPH (**Table I**). We use the principle of 4:1 to generate the training set (TS) and the internal validation set (VS) in PUTH-p1. The VS is a set for monitoring performance and mitigating overfitting during the training phase. Then, 187 patients of PUTH-p2 (N=178) without slice annotations are selected as an external test set (TeS1). The PUPH (N=87) is defined as another external test set (TeS2). The Chi-square test of distribution between the datasets reveals no significant differences among the sets (P=0.066).

TABLE I
DATASETS

Name	Num	MRI	Slice annotation	Propose
PUTH-p1	310	T2WI	√	Training and internal validation
PUTH-p2	180	T2WI		Testing
PUPH	80	T2WI		Testing
PROSTATEx	204	T2WI	√	Cross-task verification

The MRI data in our study are collected before biopsy with 3T MR scanners (Magnetom Trio, Siemens Healthcare, Erlangen, Germany; Discovery MR750, GE Healthcare, USA) without an endorectal coil. The pulse sequences consisted of T2WI is generated from axial diffusion-weighted imaging using vendor build-in software. Only DICOM data of T2WI are used for analysis in this study. For T2w sequences, we select TSE with fat suppression sequence (Siemens) or FRFSE with fat suppression sequence (GE).

The GT of PCa-GGDATA consists of two parts: GG-RP of patient-level and slice annotation. The GT of GG-RP is captured by pathological evaluation of laparoscopic RP and was reported at patient-level according to the 2016 WHO five-tier criteria [5]. Each pathology report is read and verified by two board-certified pathologists with 6 and 22 years of PCa experience, respectively. The GT of slice annotation is used to record the slices related to a pathological diagnosis in T2WI, which are tumor slices in our study. The pathologists mark the diagnosis area in the whole slide image (WSI) for GG-RP during the pathological diagnosis. Lesions belonging to these areas are then delineated in the T2WI for accurate annotation of diagnosis-related lesions. The tumor contours are manually registered from whole-mount sections to the corresponding axial T2WI slides by one board-certified urological radiologist with 12 years of experience to generate lesion annotation (**Fig. 5(a)**). The annotation of lesions help us locate the slice with pathological diagnosis-related area more accurately (**Fig. 5(b)**).

Another dataset is a publicly available dataset named the PROSTATEx, which is the set for cross-task verification from the PROSTATEx challenge [30]. Different from the PCa-GGDATA, the GT of PROSTATEx is GG-NB, which is used to evaluated model using MRI for sPCa for comparison. The slice annotation is tumor location in image, and is selected as the mask center with window size of 100×100 for tumor area in the VU. Due to the lack of GT in the test set, we use the

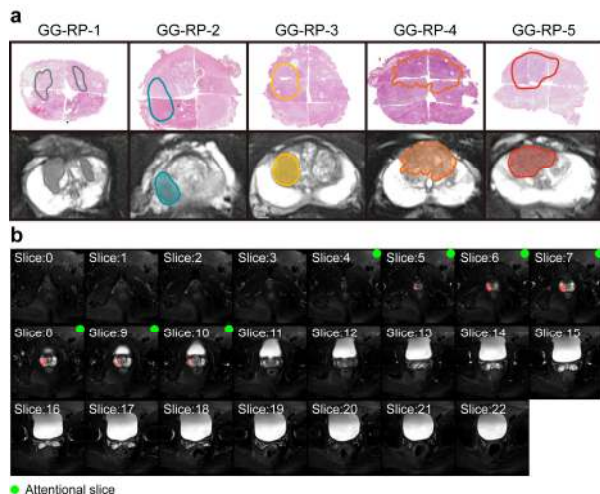training set of PROSTATEx, and evaluate models by five-fold cross-validation.

Fig. 5. Datasets illustration. (a) Tumor annotation of WSI. (b) Tumor annotations of T2WI.

V. RESULTS

A. Baseline networks for discriminating GG-RP of slice-level

First, we used tumor slices as inputs to distinguish GG-RP based on the pixel-wise analysis. GT of defined slices were copied to patients' GG-RP. Popular DCNN architectures with state-of-the-art performance on ImageNet [29] were evaluated for differentiating GG-RP in slice-level: Densenet121 [31], InceptionV3 [32], VGG16 [33], ResNet101 [34], and PNASNet [35]. The performance of DCNNs on ImageNet was reproduced by PyTorch [36]. These pretrained models were then fine-tuned to predict GG-RP at the slice-level. U-Net [37] is a popular DCNN architecture for various biomedical imaging segmentation tasks, and we reform the last layer by global average pooling combining softmax to output classification results. The models adopted the same strategy of data augmentation and condition of early-stop. The evaluations were executed by five-fold cross-validation in PUTH-p1 dataset. The results were listed in **Table II**. The best architecture of classification is the VU, which yields an accuracy of slice-level prediction (ACC-slice) of 0.628 ± 0.011. The fine-tuned model has a similar rank to ImageNet. The models with better performance on ImageNet achieves better reliability of discriminating GG-RP of slice-level. Improvements from dual attention were also be demonstrated by the ablation experiment of VU, and comparison of f1-score was shown in **Fig. 6(a)**.

To compare training strategies for GG-RP of slice-level analysis, we also used total slices to build a model with six-classification (VU-6). Normal slices, which are slices without tumor identification, were added as an extra category (the sixth category). The performance of basic architectures to six-tile classification was compared in **Table II**. Although the overall ACC-slice of VU-6 showed more outstanding than the VU, the f1-score of GG-RP was constrained. We eliminated the samples predicted to be the normal slices in the results and count the f1-score of GG-RP again, which was still not satisfactory **Fig. 6(b)**. In our experiments, the VU-6 focused on overall optimization, rather than the GG-RP, which revealed the risk of constrained

joint optimization. Therefore, we regrettably abandoned this strategy of the VU-6 to build our framework.
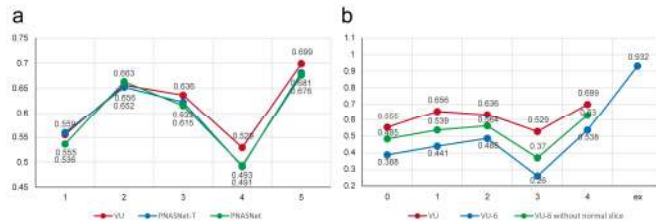

Fig. 6. (a) Accuracy of slice-level GG-RP for TOP-3 models. (b) F1-scores of GG-RP for training strategies.

B. Performance of PCa-GGNet-v2 for the patient-level prediction of GG-RP

The ACCs of patient-level prediction (ACC-case) were obtained by bootstrap (N=1000) strategy within PCa-GGDATA, and yielded ACC-case (AVG±STD) of 0.849 ± 0.023 (TS), 0.824 ± 0.051 (VS), 0.8 ± 0.029 (TeS 1), 0.824 ± 0.044 (TeS 2) respectively.

We reproduced state-of-the-art methods of PCa on the PCa-GGDATA and compared the performance of these model for GG-RP of patient-level, including evaluation of biopsy [38], radiomics [39], 3D-ResNet [40], two vote-based and 2D-DCNN models [9, 12], and our previous PCa-GGNet [27] (**Table III**). Except for radiomics-based models, all models were evaluated on the TS, VS, TeS 1, and TeS 2, respectively. Compared with clinical method of biopsy, PCa-GGNet-v2 improved the accuracy by 29.8%–39.3%. Because of the dependence of radiomics on tumor segmentation, the performance was assessed in TS and VS. SVM [41] with linear kernel, and XGBoost [42] was employed to build models using radiomic features, respectively. For vote-based 2D-DCNN models, the grade with the highest frequency of GG-RP category was determined for GG-RP of patient, which is the most commonly used modeling method for predicting patient-level indicators in MRI. Satisfactorily, the PCa-GGNet-v2 obtains the best five-classification accuracy for GG-RP of patient-level. The average computation time was calculated using two NVIDIA Titan Xp GPU with 12GB memory. We provided computation time (average prediction time per patient) in the last row of **Table III.**

C. Ablation experiments

In order to evaluate the impact of each independent unit (branch of dual attention, AU, and VU), initial input state and RWIS on the performance of the PCa-GGNet-v2, we disabled these influencing factors one by one, and used PCa-GGDATA for evaluation (**Table IV**). Firstly，we chose the random slice (rs), median slice (ms), and random slice of five layers before and after the middle layer (interval slice, is) to be the initial input for the framework, and evaluate the best starting-point of the framework. From evaluation in TS, VS, TeS 1, and TeS 2, the ms of the T2WI is the best choice with a higher ACC-case. Next, we disabled the branch of dual attention, the contribution of the performance of pixel-wise analysis-based model to the accuracy of the framework's patient-level prediction has been confirmed once again. Another significant improvement came from RWIS, the model pays more attention to the area related

TABLE II
ACCURACY (AVG±STD) OF PIXEL-WISE ANALYSIS FOR SLICE-LEVEL GG-RP IN CROSS-VALIDATION

DNN-based model	GG-RP (VU)	Overall (VU-6)	GG-RP (VU-6)
Densenet121 [31]	0.601±0.023	0.72±0.016	0.451±0.018
Inception V3 [32]	0.511±0.024	0.785±0.009	0.509±0.03
VGG16 [33]	0.434±0.037	0.787±0.014	0.508±0.021
ResNet101 [34]	0.589±0.028	0.784±0.009	0.481±0.018
PNASNet [35]	0.615±0.036	0.797±0.015	0.521±0.033
2D U-Net [37]	0.423±0.031	0.732±0.015	0.40±0.031
PNASNet+T	0.6193±0.015	0.793±0.017	0.531±0.012
VU	**0.628±0.011**	**0.797±0.007**	**0.553±0.023**

+T: Branch of tumor-level prediction; PNASNet: organ-level CNN-based model; PNASNet+T: organ+tumor-level CNN-based model; VU: organ+tumor+focal-level CNN-based model

TABLE III.
COMPARISON ACCURACY (%, AVG±STD) AND TIME COSTS (S/PATIENT, AVG) OF MODELS FOR GG-RP OF PATIENT-LEVEL

Methods	TS	VS	TeS 1	TeS 2	Time cost
Evaluation of biopsy [38]	0.478±0.031	0.519±0.064	0.502±0.038	0.431±0.057	>120
Radiomics [39]+SVM [41]	0.536±0.031	0.484±0.061	-	-	3.15
Radiomics [39]+XGBoost [42]	0.675±0.029	0.645±0.061	-	-	3.27
3D-ResNet [40]	0.73±0.029	0.643±0.061	0.574±0.035	0.615±0.052	**0.257**
Wang et. [9]	0.701±0.028	0.631±0.059	0.622±0.036	0.578±0.053	0.966
Schelb et. [12]	0.678±0.028	0.613±0.063	0.594±0.037	0.601±0.054	0.599
PNASNET (vote-based)	0.747±0.05	0.676±0.052	0.648±0.054	0.676±0.052	2.394
PCa –GGNet [27]	0.849±0.023	0.800±0.048	0.779±0.031	0.802±0.041	0.546
PCa –GGNet-v2	**0.858±0.022**	**0.824±0.051**	**0.8±0.029**	**0.824±0.044**	0.593

TABLE IV
RESULTS (AVG±STD) OF ABLATION EXPERIMENTS FOR GG-RP OF PATIENT-LEVEL

Models	TS	VS	TeS 1	TeS 2
PCa –GGNet-v2-AU (rs)	0.422±0.032	0.385±0.062	0.461±0.037	0.464±0.056
PCa –GGNet-v2-AU (ms)	0.658±0.03	0.659±0.06	0.565±0.036	0.689±0.053
PCa –GGNet-v2-AU (is)	0.633±0.031	0.582±0.063	0.52±0.037	0.622±0.054
PCa –GGNet-v2 -TL	0.832±0.024	0.789±0.052	0.778±0.032	0.802±0.045
PCa –GGNet-v2-FL-TL	0.847±0.023	0.805±0.049	0.779±0.031	0.813±0.044
PCa –GGNet-v2-RWIS	0.782±0.026	0.696±0.058	0.666±0.034	0.687±0.052
PCa –GGNet-v2	**0.858±0.022**	**0.824±0.051**	**0.8±0.029**	**0.824±0.044**

rs, random slice; ms, median slice; is, interval slice; TL, branch of tumor-level; FL, branch of focal-level.

to GG-RP of patient in the joint optimization by reconsidering the importance of slices in the training process of the VU.

D. HyperParameter sensitivity analysis

In our experiments, the hyperparameter selection was based on the performance of the validation set during the training process, which was independent of multi-center dataset validation. The hyperparameters of branch weight (α, β), effect of impression weight λ, and iteractions of RWIS were selected by slice-level results of cross-validation, and action list $\mathbb{A}$ and circle t were determined by patient-level results of the VC. Sensitivity to hyperparameters of the VU was listed in **Table V** and heperparameters of the AU was listed in **Tabel VI**, and **Tabel VII**. Finally, We chose the optimal hyperparameter combination in the experiments to construct PCa-GGNet-v2. More details was listed in **Supplementary Materials**. From the results of sensitivity analysis, the performance of PCa-GGNet-v2 is mainly contributed to hyperparameters of the action list and the number of circles in the AU. Suitable hyperparameters settings of the VU also brought a slight improvement. The existence of hyperparameters provides more flexibility for the framework, which is hopeful for expansion in different tasks, but it also requires more experiments.

E. Process visualization and interpretability

To illustrate the forward process of PCa-GGNet-v2 for end-to-end predicting GG-RP of patients, five typical cases were shown for visualization and interpretation (**Fig. 7**). The results demonstrated the robustness of the model under circumstances of different initial slices, single or multifocal lesions, different termination-action status, and decision paths. This process follows the diagnostic logic of radiologists and presents the image-based association ability of the model. The decision slices from the model also implied the risk area of PCa for significant tumor detection by the red area in heatmap.

F. Performance of PCa-GGNet-v2 for sPCa detection

We retrained the PCa-GGNet-v2 using PROSTATEx for sPCa detection, and evaluated by five-fold cross-validation. Four popular methods for sPCa and our previous work were employed for comparison under the same experimental conditions. The 2D DCNN-based models [9, 12, 43] were trained by weakly supervised learning and integrate the results of patients by vote-based strategy. The evaluation indicators are the accuracy of slice-level and patient-level (**Table VIII**). Patient-level performance logically relied on results from slices, but still depended on a better integration strategy. Additionally, improvements of the VU with dual attention was also demonstrated by ACC-slice. The PCa-GGNet-v2 keeps the state-of-the-art performance of patient-level against other models, including models with multi-modality inputs, which our model excavates more useful information related to diagnosis in both the slice-level and patient-level analysis.

This article has been accepted for publication in a future issue of this journal, but has not been fully edited. Content may change prior to final publication. Citation information: DOI 10.1109/TBME.2021.3082176, IEEE Transactions on Biomedical Engineering

9

TABLE V
SENSITIVITY TO HYPERPARAMETERS IN THE VU

(α, β)	ACC-slice	λ	ACC-slice	I_{RWIS}	ACC-slice
(0,0)	0.615±0.036	1	0.613±0.021	0	0.628±0.011
(1,0)	0.619±0.037	0.9	0.614±0.020	1	0.659±0.012
(0,1)	0.607±0.04	0.5	0.622±0.019	2	0.669±0.011
(1,1)	0.623±0.014	0.2	0.624±0.015	3	0.670±0.014
(0.1,1)	0.611±0.023	**0.09**	**0.628±0.011**	4	**0.673±0.014**
(1,0.1)	0.621±0.017	0.05	0.627±0.012	5	0.671±0.013
(0.1,0.1)	**0.628±0.011**	0.02	0.628±0.012	6	0.669±0.012
(0.01,0.01)	0.619±0.020	0	0.625±0.019	7	0.669±0.013

I_{RWIS}: Iteraction of RWIS

TABLE VI
SENSITIVITY TO ACTION LIST IN THE AU

	TS		VS		TeS1	TeS2
	ACC-tumor	ACC-case	ACC-tumor	ACC-case	ACC-case	ACC-case
Type A	0.854±0.022	0.772±0.025	0.804±0.071	0.77±0.077	0.71±0.028	0.703±0.027
Type B	0.85±0.021	**0.86±0.02**	**0.839±0.068**	0.8±0.076	0.783±0.031	0.82±0.028
Type C	**0.864±0.02**	0.858±0.022	0.834±0.068	**0.824±0.051**	**0.8±0.029**	**0.824±0.044**

Type A, $\mathbb{A} = \{0, +1, -1\}$; Type B, $\mathbb{A} = \{0, +1, -1, +2, -2\}$; Type C, $\mathbb{A} = \{0, +1, -1, +2, -2, +3, -3\}$

TABLE VII
SENSITIVITY TO CIRCLES OF THE PCA-GGNET-V2

	TS		VS		TeS1	TeS2	Time costs
	ACC-tumor	ACC-case	ACC-tumor	ACC-case	ACC-case	ACC-case	(s/ patient)
1	0.671±0.028	0.658±0.03	0.684±0.029	0.659±0.06	0.565±0.036	0.689±0.053	**0.136**
2	0.89±0.019	0.716±0.027	0.798±0.075	0.735±0.082	0.622±0.037	0.688±0.052	0.279
3	**0.9±0.017**	0.81±0.023	0.821±0.067	0.765±0.079	0.766±0.032	0.747±0.05	0.519
4	0.864±0.02	**0.858±0.022**	**0.834±0.068**	0.824±0.051	**0.8±0.029**	**0.824±0.044**	0.401
5	0.888±0.019	0.879±0.023	0.766±0.076	**0.834±0.068**	0.773±0.031	0.811±0.044	0.541
6	0.837±0.022	0.88±0.021	0.832±0.069	0.801±0.075	0.715±0.034	0.787±0.047	0.795
7	0.885±0.019	0.86±0.023	0.763±0.073	0.732±0.081	0.725±0.032	0.762±0.047	1.03

ACC-tumor, accuracy of slice with tumor in the final decision slices.

TABLE VIII
PERFORMANCE OF MODEL FOR VALIDATION SET OF CROSS-VALIDATION IN PROSTATEX DATASET

	Modality	ACC-slice	ACC-case
Wang et. [9]	T2-tra+ADC	**0.761±0.011**	0.755±0.025
Schelb et. [12]	T2-tra	0.674±0.020	0.6727±0.033
Wang et. [43]	T2-tra	0.604±0.013	0.64±0.046
3D-ResNet [40]	T2-tra	-	0.725±0.022
PCa –GGNet	T2-tra	0.697±0.014	0.783±0.028
PCa –GGNet-v2	T2-tra	0.715±0.015	**0.804±0.026**

VI. DISCUSSION

This work is inspired by artificial intelligence of the e-sports game proposed by Mnih et al.[20]: the goal of our game is to find which slices should be observed and construct the best individual prediction based on these findings. The 3D image block of a patient is defined as a game, and each slice of images is a frame of the game process.

We aim to learn diagnostic logic from radiologists for MRI of PCa, which searching diagnosis-related slices to construct a patient-level prediction of variant pathological behavior. We define the patient-level prediction based on pixel-wise analysis as a decision path optimization problem, and used joint optimization. We propose an end-to-end framework (PCa-GGNet-v2) mimicking this process by combining both DCNN and DRL for GG-RP of patient-level, which is a multi-classification task. The AU, which is trained by interactions with the environment to maximize cumulative reward signals. Inputs are switched by the response of the AU with current image features. The AU finds attentional slices from T2WI, and identifies a patient-level prediction of GG-RP, mimicking radiologists' behavior. To enhance features related to GT in pixel-wise analysis, we adopt the VU with dual attention with weakly supervised learning to encode images and achieve slice-level prediction with high accuracy.

For patient-level, we abandon the vote-based strategies (which use the results at the slice-level to transform the prediction results from the slice-level to the patient-level) because of their limited accuracy, suboptimal interpretability, and insufficient decision basis. Compared with the results of previous DCNN-based models using majority-vote strategy [9, 15], our method achieved better performance in patient-level prediction. Previous researchers mainly focused on slice-level analysis rather than the patient-level problem. Except for the DCNN-based model, Cameron et al. [44] and Chaddad et al. [45] employed radiomics-based method to predict GG of PCa. These works rely on tumor delineation. For comparison, our framework does not depend on tumor masks, which reduces the error derived from the original segmentation. In the experiment, our proposed method outperformed DCNN (p-value<0.05) and radiomics (p-value<0.05) significantly. Overfitting is also mitigated properly. Compared with our previous work, we update the method of pixel-wise analysis by dual attention strategy and RWIS for weakly supervised learning. Significant improvements are revealed in both in-house multi-center dataset (PCa-GGDATA) and public dataset (PROSTATEx), in which the evolution and generalization of the method is proven.

During weakly supervised learning of the VU in PCa-GGNet-V2, it may be risky to apply individual assessment directly as each slice's GT during the supervised training because of asymmetric information. Specifically, it means that a low-level holistic assessment (individual, at the patient-level) is applied indiscriminately to a high-level detailed assessment

(each slice, at the slice-level), which may interfere with the model fitting and increase the risk of overfitting. Therefore, we define a set of attentional slices as the decision path, in which these slices are considered more by the framework to maximize prediction accuracy. We use the decision path to re-weight the importance of slices in the weakly supervised learning to weaken the fitting risk brought by the usage of asymmetric GT.

In the future, we tend to combine inter-slice spatial contexts as an additional reference of slice selection and design a better DRL-based model with richer actions. Next, we hope to add more sequences to realize an mp-MRI-based framework and improve accuracy. Additionally, we plan to implement lesion detection and segmentation during the prediction, to help clinicians understand the decision logic of the model and improve the interpretability of the method.
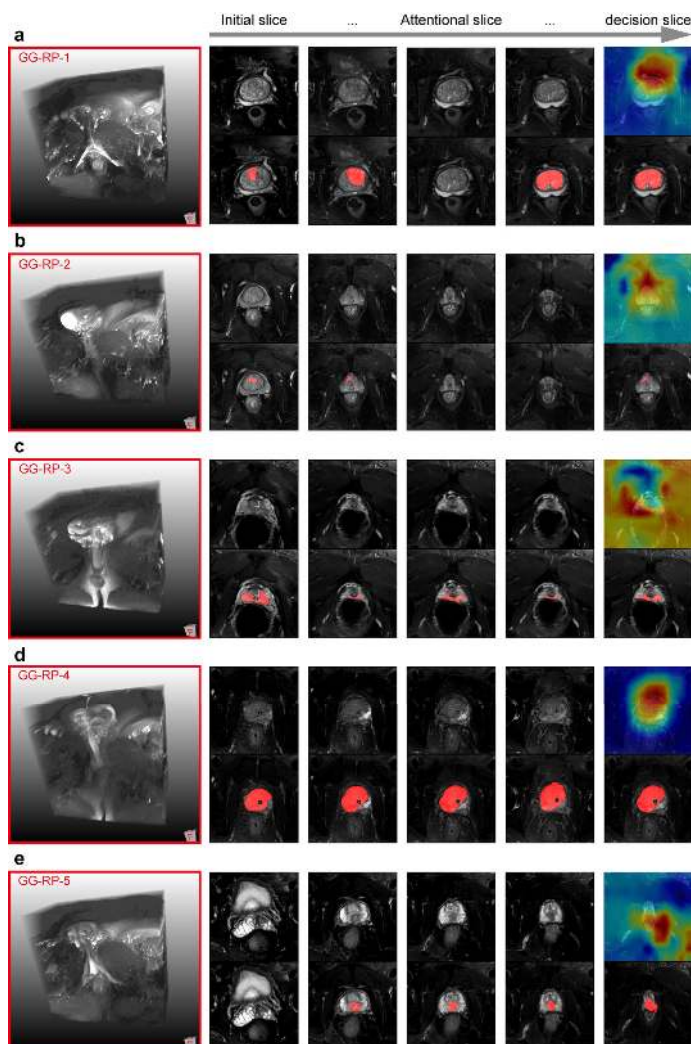

Fig. 7. PCa-GGNet-v2 for GG-RP of patients. The first column shows the 3D preview of T2WI. The first row of second to sixth columns show the selected images as inputs and their predicted probabilities. The second row shows the real tumor location according to postoperative pathology.

VII. CONCLUSION

In this paper, we propose the PCa-GGNet-v2 for end-to-end predicting multi-classification task at the patient-level, and achieve state-of-the-art performance in both multi-center dataset and public dataset for variant clinical applications. The

PCa-GGNet-v2 is designed to learn from radiologists to form slice-level findings to a patient-level decision, which realize joint optimization and avoid the risk of asymmetric use of GT. We also believe that our method can provide more accurate pathological evaluations for real clinical practice of PCa and provide a new path for patient-level tasks based on 3D images with low resolution of inter-slice.

REFERENCES

[1] R. L. Siegel, K. D. Miller, and A. Jemal, "Cancer statistics, 2019," *CA: a cancer journal for clinicians,* vol. 69, no. 1, pp. 7-34, 2019.

[2] J. I. Epstein *et al.*, "A contemporary prostate cancer grading system: a validated alternative to the Gleason score," *European urology,* vol. 69, no. 3, pp. 428-435, 2016.

[3] P. A. Humphrey, "Gleason grading and prognostic factors in carcinoma of the prostate," *Modern pathology,* vol. 17, no. 3, pp. 292-306, 2004.

[4] J. L. Mohler *et al.*, "Prostate cancer, version 2.2019, NCCN clinical practice guidelines in oncology," *Journal of the National Comprehensive Cancer Network,* vol. 17, no. 5, pp. 479-505, 2019.

[5] J. I. Epstein, W. C. Allsbrook Jr, M. B. Amin, L. L. Egevad, I. S. U. P. G. Committee, and others, "The 2005 International Society of Urological Pathology (ISUP) consensus conference on Gleason grading of prostatic carcinoma," *The American journal of surgical pathology,* vol. 29, no. 9, pp. 1228-1242, 2005.

[6] J. I. Epstein, Z. Feng, B. J. Trock, and P. M. Pierorazio, "Upgrading and downgrading of prostate cancer from biopsy to radical prostatectomy: incidence and predictive factors using the modified Gleason grading system and factoring in tertiary grades," *European urology,* vol. 61, no. 5, pp. 1019-1024, 2012.

[7] D. Danneman *et al.*, "Accuracy of prostate biopsies for predicting Gleason score in radical prostatectomy specimens: nationwide trends 2000--2012," *Bju International,* vol. 119, no. 1, pp. 50-56, 2017.

[8] A. R. Padhani, J. Weinreb, A. B. Rosenkrantz, G. Villeirs, B. Turkbey, and J. Barentsz, "Prostate imaging-reporting and data system steering committee: PI-RADS v2 status update and future directions," *European urology,* vol. 75, no. 3, pp. 385-396, 2019.

[9] Z. Wang, C. Liu, D. Cheng, L. Wang, X. Yang, and K.-T. Cheng, "Automated detection of clinically significant prostate cancer in mp-MRI images based on an end-to-end deep neural network," *IEEE transactions on medical imaging,* vol. 37, no. 5, pp. 1127-1139, 2018.

[10] Y. Shao, J. Wang, B. Wodlinger, and S. E. Salcudean, "Improving Prostate Cancer (PCa) Classification Performance by Using Three-Player Minimax Game to Reduce Data Source Heterogeneity," *IEEE Transactions on Medical Imaging,* 2020.

[11] S. Srivastava *et al.*, "Cancer overdiagnosis: a biological challenge and clinical dilemma," *Nature Reviews Cancer,* vol. 19, no. 6, pp. 349-358, 2019.

[12] P. Schelb *et al.*, "Classification of cancer at prostate MRI: deep learning versus clinical PI-RADS assessment," *Radiology,* vol. 293, no. 3, pp. 607-617, 2019.

[13] Q. Liu, Q. Dou, L. Yu, and P. A. Heng, "Ms-net: Multi-site network for improving prostate segmentation with heterogeneous mri data," *IEEE Transactions on Medical Imaging,* 2020.

[14] Y. Guo, Y. Gao, and D. Shen, "Deformable MR prostate segmentation via deep feature learning and sparse patch matching," *IEEE transactions on medical imaging,* vol. 35, no. 4, pp. 1077-1089, 2015.

[15] R. Cao *et al.*, "Joint prostate cancer detection and gleason score prediction in mp-MRI via FocalNet," *IEEE transactions on medical imaging,* vol. 38, no. 11, pp. 2496-2506, 2019.

[16] N. Ghavami *et al.*, "Automatic segmentation of prostate MRI using convolutional neural networks: Investigating the impact of network architecture on the accuracy of volume measurement and MRI-ultrasound registration," *Medical image analysis,* vol. 58, p. 101558, 2019.

[17] S. Alley, A. Fedorov, C. Menard, and S. Kadoury, "Evaluation of intensity-based deformable registration of multi-parametric MRI for radiomics analysis of the prostate," in *Medical Imaging 2020:*

Biomedical Applications in Molecular, Structural, and Functional Imaging, 2020, vol. 11317, p. 113171H.

[18] X. Yang *et al.*, "Co-trained convolutional neural networks for automated detection of prostate cancer in multi-parametric MRI," *Medical image analysis,* vol. 42, pp. 212-227, 2017.

[19] S. Wang and R. M. Summers, "Machine learning and radiology," *Medical image analysis,* vol. 16, no. 5, pp. 933-951, 2012.

[20] V. Mnih *et al.*, "Human-level control through deep reinforcement learning," *nature,* vol. 518, no. 7540, pp. 529-533, 2015.

[21] A. Alansary *et al.*, "Evaluating reinforcement learning agents for anatomical landmark detection," *Medical image analysis,* vol. 53, pp. 156-164, 2019.

[22] G. Maicas, G. Carneiro, A. P. Bradley, J. C. Nascimento, and I. Reid, "Deep reinforcement learning for active breast lesion detection from DCE-MRI," in *International conference on medical image computing and computer-assisted intervention*, 2017, pp. 665-673.

[23] G. Maicas, A. P. Bradley, J. C. Nascimento, I. Reid, and G. Carneiro, "Pre and post-hoc diagnosis and interpretation of malignancy from breast DCE-MRI," *Medical Image Analysis,* vol. 58, p. 101562, 2019.

[24] Z. Liu *et al.*, "The applications of radiomics in precision diagnosis and treatment of oncology: opportunities and challenges," *Theranostics,* vol. 9, no. 5, p. 1303, 2019.

[25] D. Bonekamp *et al.*, "Radiomic machine learning for characterization of prostate lesions with MRI: comparison to ADC values," *Radiology,* vol. 289, no. 1, pp. 128-137, 2018.

[26] J. C. Weinreb *et al.*, "PI-RADS prostate imaging--reporting and data system: 2015, version 2," *European urology,* vol. 69, no. 1, pp. 16-40, 2016.

[27] L. Shao *et al.*, "Radiologist-like artificial intelligence for grade group prediction of radical prostatectomy for reducing upgrading and downgrading from biopsy," *Theranostics,* vol. 10, no. 22, p. 10200, 2020.

[28] R. S. Sutton and A. G. Barto, *Reinforcement learning: An introduction*. MIT press, 2018.

[29] J. Deng, W. Dong, R. Socher, L.-J. Li, K. Li, and L. Fei-Fei, "Imagenet: A large-scale hierarchical image database," in *2009 IEEE conference on computer vision and pattern recognition*, 2009, pp. 248-255.

[30] G. Litjens, O. Debats, J. Barentsz, N. Karssemeijer, and H. Huisman, "Computer-aided detection of prostate cancer in MRI," *IEEE transactions on medical imaging,* vol. 33, no. 5, pp. 1083-1092, 2014.

[31] G. Huang, Z. Liu, G. Pleiss, L. Van Der Maaten, and K. Weinberger, "Convolutional networks with dense connectivity," *IEEE transactions on pattern analysis and machine intelligence,* 2019.

[32] C. Szegedy, V. Vanhoucke, S. Ioffe, J. Shlens, and Z. Wojna, "Rethinking the inception architecture for computer vision," in *Proceedings of the IEEE conference on computer vision and pattern recognition*, 2016, pp. 2818-2826.

[33] K. Simonyan and A. Zisserman, "Very deep convolutional networks for large-scale image recognition," *arXiv preprint arXiv:1409.1556,* 2014.

[34] S. Xie, R. Girshick, r. Doll\'a, Piotr, Z. Tu, and K. He, "Aggregated residual transformations for deep neural networks," in *Proceedings of the IEEE conference on computer vision and pattern recognition*, 2017, pp. 1492-1500.

[35] C. Liu *et al.*, "Progressive neural architecture search," in *Proceedings of the European Conference on Computer Vision (ECCV)*, 2018, pp. 19-34.

[36] A. Paszke *et al.*, "Automatic differentiation in pytorch," 2017.

[37] O. Ronneberger, P. Fischer, and T. Brox, "U-net: Convolutional networks for biomedical image segmentation," in *International Conference on Medical image computing and computer-assisted intervention*, 2015, pp. 234-241.

[38] S. Loeb, Y. Folkvaljon, D. Robinson, I. F. Lissbrant, L. Egevad, and P. a. Stattin, r, "Evaluation of the 2015 Gleason grade groups in a nationwide population-based cohort," *European urology,* vol. 69, no. 6, pp. 1135-1141, 2016.

[39] J. J. M. Van Griethuysen *et al.*, "Computational radiomics system to decode the radiographic phenotype," *Cancer research,* vol. 77, no. 21, pp. e104-e107, 2017.

[40] K. Hara, H. Kataoka, and Y. Satoh, "Learning spatio-temporal features with 3D residual networks for action recognition," in *Proceedings of the IEEE International Conference on Computer Vision Workshops*, 2017, pp. 3154-3160.

[41] C. Cortes and V. Vapnik, "Support-vector networks," *Machine learning,* vol. 20, no. 3, pp. 273-297, 1995.

[42] T. Chen and C. Guestrin, "Xgboost: A scalable tree boosting system," in *Proceedings of the 22nd acm sigkdd international conference on knowledge discovery and data mining*, 2016, pp. 785-794.

[43] Y. Wang and M. Wang, "Selecting proper combination of mpMRI sequences for prostate cancer classification using multi-input convolutional neuronal network," *Physica Medica,* vol. 80, pp. 92-100, 2020/12/01/ 2020.

[44] A. Cameron, F. Khalvati, M. A. Haider, and A. Wong, "MAPS: a quantitative radiomics approach for prostate cancer detection," *IEEE Transactions on Biomedical Engineering,* vol. 63, no. 6, pp. 1145-1156, 2015.

[45] A. Chaddad, M. J. Kucharczyk, and T. Niazi, "Multimodal radiomic features for the predicting gleason score of prostate cancer," *Cancers,* vol. 10, no. 8, p. 249, 2018.